IEEE Access
Multidisciplinary ⋮ Rapid Review ⋮ Open Access Journal

Date of publication xxxx 00, 0000, date of current version xxxx 00, 0000.

Digital Object Identifier 10.1109/ACCESS.2017.Doi Number

Dental-YOLO: Alveolar Bone and Mandibular Canal Detection on Cone Beam Computed Tomography Images for Dental Implant Planning

MONICA WIDIASRI[1,2], (Member, IEEE), AGUS ZAINAL ARIFIN[1], NANIK SUCIATI[1], (Member, IEEE), CHASTINE FATICHAH[1], (Member, IEEE), EHA RENWI ASTUTI[3], RARASMAYA INDRASWARI[4], (Member, IEEE), RAMADHAN HARDANI PUTRA[3], AND CHOIRU ZA'IN[5]

[1]Department of Informatics, Faculty of Intelligent Electrical and Informatics Technology, Institut Teknologi Sepuluh Nopember, Surabaya 60111, Indonesia

[2]Department of Informatics, Faculty of Engineering, Universitas Surabaya, Surabaya 60293, Indonesia

[3]Department of Dentomaxillofacial Radiology, Faculty of Dental Medicine, Universitas Airlangga, Surabaya 60131, Indonesia

[4]Department of Information Systems, Faculty of Intelligent Electrical and Informatics Technology, Institut Teknologi Sepuluh Nopember, Surabaya 60111, Indonesia

[5]Faculty of Information Technology, Monash University, Clayton VIC 3800, Australia

Corresponding author: Nanik Suciati (e-mail: nanik@if.its.ac.id)

This work was supported by the Directorate General of Higher Education, Ministry of Education and Culture of the Republic of Indonesia for PDD (Doctoral Dissertation Research) 2020-2021 with grant number 008/E5/PG.02.00.PT/2022 and the University of Surabaya for a doctoral program scholarship with number 1151/PKD-SL/SDM/VIII/2020.

ABSTRACT In planning a mandibular posterior dental implant, identifying the exact location of the alveolar bone (AB) and mandibular canal (MC) is essential to determine the height and width of the available bone. Cone beam computed tomography (CBCT) is a 3D imaging modality widely used for dental implant planning, which requires a lower radiation dose compared to medical CT and can provide cross-sectional image quality to visualize AB and MC. The radiologist carried out the AB and MC detection processes manually on each section of the CBCT image until the appropriate area was determined for bone measurement. This process is time consuming, and the measurement accuracy depends on the ability and experience of the radiologist. This study proposes an automatic and simultaneous detection system for AB and MC based on 2D grayscale CBCT images, that can simplify and expedite dental implant planning. We introduce Dental-YOLO, an efficient version of YOLOv4 specifically developed to detect AB and MC, with two-scale feature maps at low and high scales. The height and width of the available bone in the implant area were estimated by using the detected bounding box attributes. The AB and MC detection performances using Dental-YOLO reached a mean average precision of 99.46%. The two-way analysis of variance (ANOVA) test showed no difference in the bone height and width measurements produced by the proposed approach and manual measurement by radiologists. Our results suggest that the Dental-YOLO detection system could be helpful for dental implant surgery and presurgical treatment planning.

INDEX TERMS Alveolar bone, CBCT, bone measurement, dental implant planning, mandibular canal, object detection, YOLO.

I. INTRODUCTION

Dental implants are artificial tooth roots implanted in the jawbone to replace the lost teeth. Presurgical treatment planning is required to determine the ideal implant dimension and position to ensure long-term success and reduce the risks associated with dental implant surgery. Cone beam computed tomography (CBCT) has been widely used

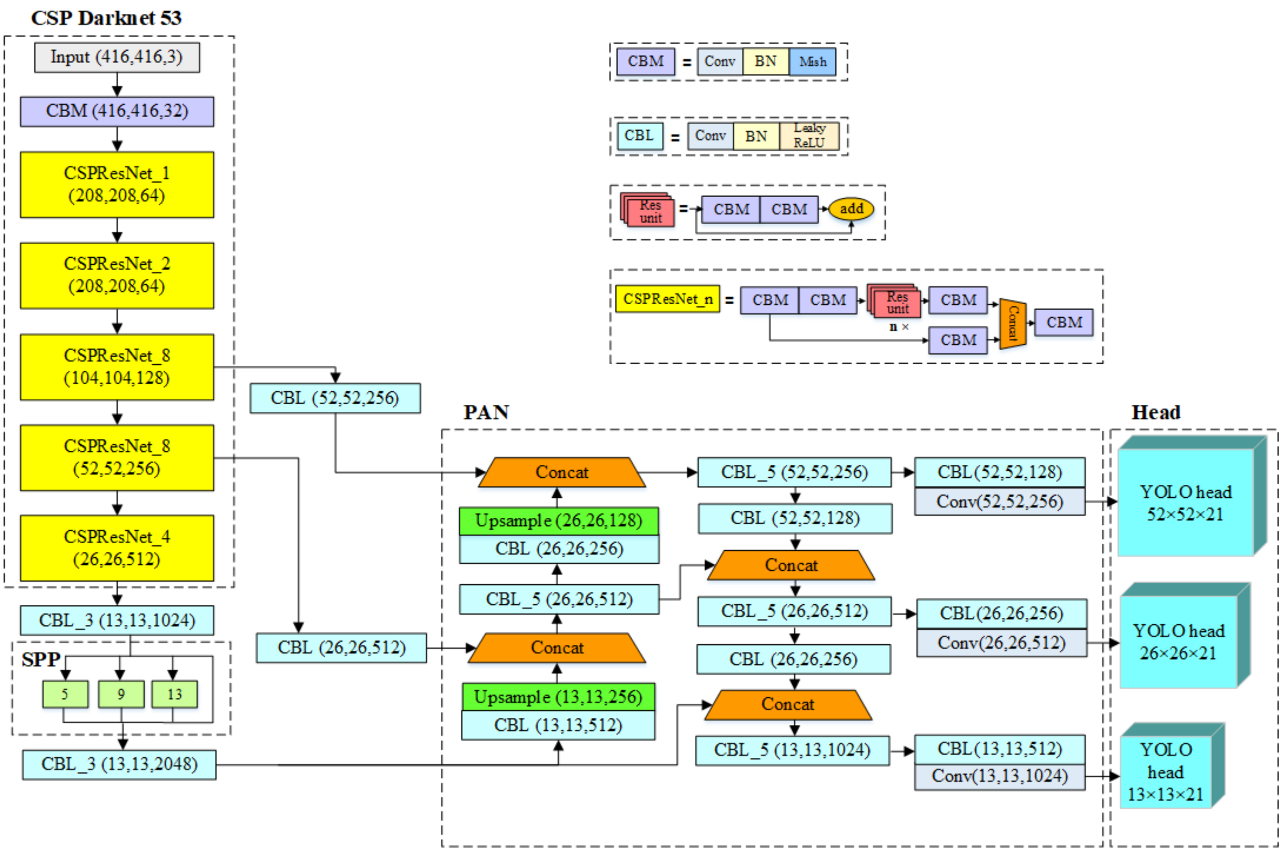

FIGURE 1. YOLOv4 architecture.

in implant dentistry because of its advantages in providing anatomical information as well as three-dimensional (3D) images of roots [1], bones [1][2], nerves [1], and crucial structures in the implantation site [1][2]. Thus, CBCT helps in dental implant planning to improve treatment outcomes by providing essential information on ideal implant dimensions and positions according to the available bone [3].

Dental implant placement in the mandibular posterior site should consider the location of the mandibular canal (MC) as a crucial structure [4][5]. The MC was identified manually in each cross-section of the CBCT images, followed by manual bone height and width measurements by a radiologist using a 3D imaging software. The width and height of the alveolar bone (AB) are essential for determining the implant dimensions. Identifying the MC and measuring the bone is time-consuming and labor-intensive. Furthermore, the accuracy of the measurement depends on the radiologist's expertise and experience in interpreting CBCT images [6][7].

Deep learning has progressed rapidly and has achieved significantly higher accuracy than traditional machine learning because it can extract high-dimensional features automatically [8]. Deep learning-based approaches can significantly reduce the time and mistakes carried out by inexperienced radiologists in interpreting the medical images in their daily clinical practice. The deep learning approach was initially implemented in dental radiology research [9]. Deep learning has been used to successfully detect bone radiography levels in panoramic radiographs [10], localize the MC on CBCT volume [6], classify teeth on CBCT images [11], segment AB on CBCT images [12], segment the mandibular cortical bone [13], MC [14][15], tooth [12][16][17], and inferior alveolar nerve [18] on CBCT images.

Mandibular dental implant planning requires detection or segmentation of the AB and MC. Cui et al. proposed automatic tooth and alveolar bone segmentation on 3D CBCT images using the V-Net method which is a 3D fully CNN [12]. The accuracy of the alveolar bone segmentation in that study reached a Dice value of 94.5%. Research on alveolar bone segmentation with a deep learning approach that uses CBCT images has not been done much. Opportunities are available to conduct studies on AB segmentation using CBCT images. Jaskari et al. proposed a deep learning approach to automatically locate MC in CBCT images using a 3D fully CNN [6]. The MC localization accuracy was 0.90. The result can reduce the manual process of annotating MC. Kwak et al. proposed a deep learning approach based on two-dimensional (2D) SegNet, 2D U-Nets, and 3D U-Nets to automatically segment the MC on CBCT images [14]. Experiments with training using pre-training weights showed better segmentation results, and the segmentation accuracy of 3D U-Net model was the best, with a global accuracy of 0.99. These results contribute significantly to dental implant planning. U-Net 3D architecture is also used for MC segmentation on AI-driven modules [15]. This study demonstrated a new, fast, and accurate AI-based module for MC segmentation in CBCT. However, studies that simultaneously and automatically detect AB and MC have not yet been widely established. Thus, there are many opportunities for accurate autodetection using deep learning to detect both objects.

YOLO, a state-of-the-art detection system based on deep learning, is a single-stage CNN detector that simultaneously makes object localization and classification predictions [19] with high detection accuracy and speed [8]. In object detection, many bounding boxes and their classifications must be drawn around the object. There are different versions of YOLO: YOLOv2 [20], YOLOv3 [21], and YOLOv4 [22]. To analyze medical images, YOLO was used to localize and track the myocardial wall from cardiac flow-field ultrasound images [23] and to automatically detect COVID-19 from raw chest X-ray images [24]. YOLOv3 was used to detect breast masses in full-field digital mammograms [25], and YOLOv4 was used to successfully detect melanoma lesions [26]. In dentistry, YOLOv3 has been successfully used to detect dental caries on digital bite radiographs [9], and YOLOv3-tiny has been successfully used to detect AB [27]. Therefore, YOLO is appropriate for dental implant planning, and in this case, for the simultaneous detection of AB and MC.

The YOLO detector consists of three main parts: backbone, neck, and head components. All object detectors take an image as input and compress the features down through the backbone of the CNN. In the neck, a combination of backbone features occurs in the layers. The head section detects an object by creating an object bounding box, predicting the object class, and determining the location of the object. YOLOv4 consists of a cross-stage partial (CSP) Darknet53 as the backbone network, spatial pyramid pooling (SPP) module, PANet as the neck network, and YOLOv3 as the head, which uses a three-scale feature map at the head to predict the detection results [22]. The CSP Darknet53 consists of a convolution building block (CBM) and five CSPResNet modules. The CBM contains a convolution layer (Conv), batch normalization layer, and Mish layer. CSPResNet is a convolutional neural network with a CSP approach that is applied to ResNet. Fig. 1 shows the YOLOv4 architecture. In the YOLOv4 architecture, three-scale feature maps (low, medium, and high) are used to detect objects of various sizes. In dental implant planning, simultaneous detection of AB and MC is required for the measurement of available bone in the implant area. AB can be easily detected because of its large size, whereas MC is more difficult to detect because of its small size. Detection using YOLOv4 to specifically detect AB and MC, which have large differences in size, may be less efficient. Therefore, it is crucial to provide appropriate feature maps on the YOLOv4 architecture to increase the detection efficiency of AB and MC.

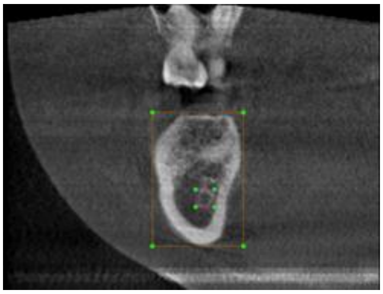

FIGURE 2. Annotation of the mandibular canal and alveolar bone on coronal slice.

This study proposes an automatic and simultaneous detection system for AB and MC based on 2D grayscale CBCT images that can simplify and expedite dental implant planning. We introduce Dental-YOLO, an efficient version of YOLOv4 specifically developed to detect AB and MC, with two-scale feature maps at low and high scales. A low-scale feature map is more efficient in detecting relatively large AB objects, whereas a high-scale feature map is more efficient at detecting much smaller MC objects. The detected bounding box attribute was then used to measure the available bone height and width in the implant area. The proposed detection system can produce bone quantity measurement, which is very important in dental implants.

II. METHODOLOGY

A. DATASETS

This study used 2D grayscales CBCT images of the coronal slices of the mandible. The images were annotated to create ground-truth images using LabelImg, a graphic annotation tool. The annotation process was performed by creating bounding boxes for each image's AB and MC objects. Fig. 2 shows an example of annotating AB and MC objects from the coronal slice. The AB annotations are depicted as a yellow box, and the MC annotations are depicted as a purple box. A text file in YOLO format for each image was generated containing the class number, center coordinate values, and the width and height of the bounding box relative to the image width and height for each object.

The CBCT dental images were obtained from Universitas Airlangga Academic Dental Hospital. All images were obtained using CBCT OP300 3D scanner (Instrumentarium Dental, Tuusula, Finland). The experiment used 1064 2D

TABLE I
DISTRIBUTION OF THE DATA

Method	Total images	No. of annotations	
		AB	MC
Training	744	773	402
Testing	320	330	173
Total	**1064**	**1103**	**575**

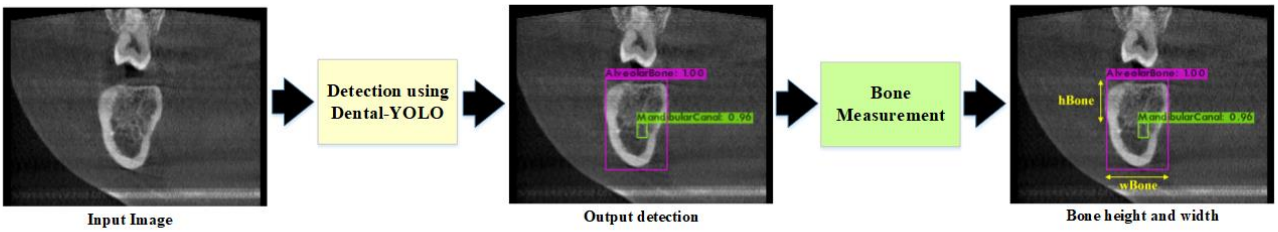

FIGURE 3. Sytem workflow.

CBCT images of coronal slices, divided into 70% for training and 30% for testing. The training process used 744 images and 320 images for the testing process. 1678 annotations were made, consisting of 1103 AB and 575 MC annotations. A radiologist with 14 years of professional experience validated the annotation results. Table I shows the distribution of the images and annotations used in this study.

B. SYSTEM OVERVIEW

To detect AB and MC objects, the image and ground truth that were developed are used as inputs to train and test Dental-YOLO. The Dental-YOLO model accepts an input image of size 416 × 416 pixels. Dental-YOLO training and testing used pre-prepared training and testing datasets. The detection results are shown as a bounding box, class name, and detection confidence value for the detected object. The class names used in this study were AB for the alveolar bone and MC for the mandibular canal. The detection confidence value ranges from 0.00 to 1.00, where 1.00 represents the highest level of detection confidence. The height and width of the available bone in the implant area were measured using the coordinates, length, and width of the bounding box obtained from Dental-YOLO detection. Fig. 3 shows the workflow of the system. The detection performance of Dental-YOLO was examined by comparing the detection results with those of a comparison detector. The measurements of bone height and width using the proposed approach were compared with the manual measurements conducted by two radiologists.

C. Dental-YOLO

The Dental-YOLO network model is specifically designed to detect AB and MC by making the YOLOv4 network model more efficient in the training and detection processes. Fig. 4 shows the Dental-YOLO architecture. Dental-YOLO uses a CSP Darknet53-tiny network as the backbone network. The CSP Darknet53-tiny consists of three convolution networks, batch normalization, LeakyReLU activation function (CBL) layers, and three CSP modules. The CSP Darknet53-tiny network uses the CSP module instead of the CSPResNet module used in CSP Darknet53. The CSP module can improve convolution network learning ability compared with the

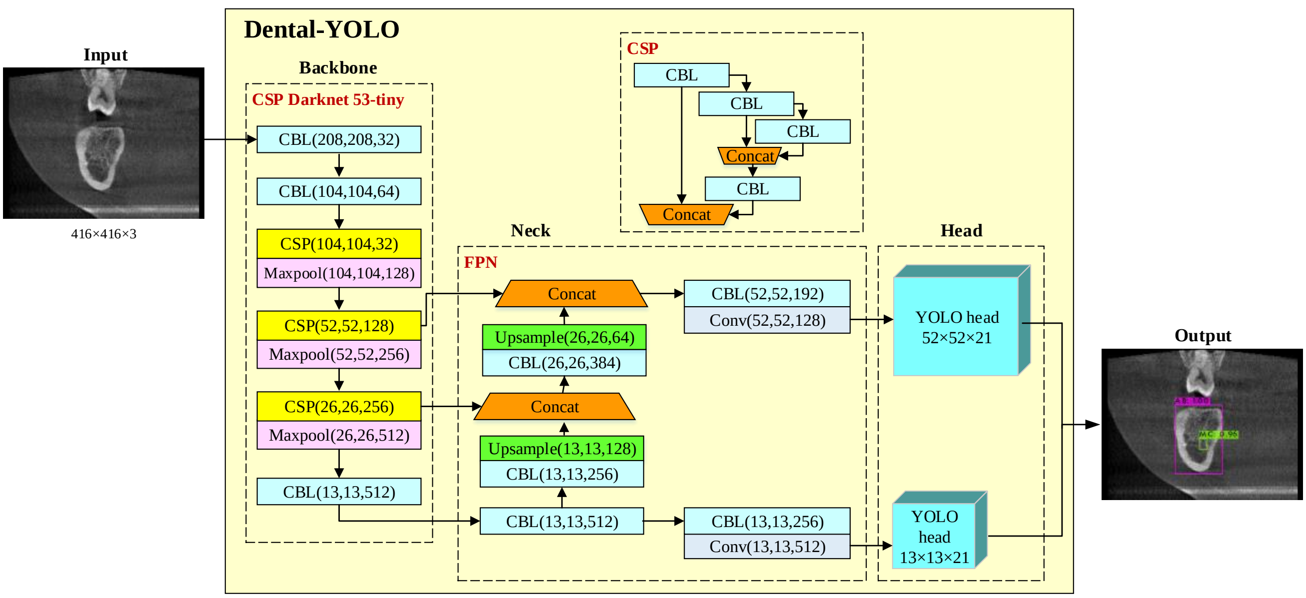

FIGURE 4. Dental-YOLO.

ResNet module [28]. The CSP network strategy reduces the computational complexity by dividing the feature map from the base layer into two parts and then combining them through a cross-stage hierarchy. In addition, CSPDarknet53-tiny uses the LeakyReLU activation function in the CSP module to simplify the computational process [28]. The maxpool layer is added after the CSP module to maintain the resolution of the feature map. Simplification of this backbone network can lead to a faster training process. In the feature fusion section of the neck network, the Dental-YOLO approach uses a feature pyramid network (FPN) to extract feature maps with different scales. The FPN combines top-down path convolution networks and lateral connections to develop high-level semantic feature maps at all scales [29]. An FPN can enhance object detection speed with high detection accuracy. Dental-YOLO uses two-scale feature maps on the head to predict the detection results, making it more efficient in detecting two objects.

To better detect AB and MC, we used two-scale feature maps of low and high scales. Because AB objects can be detected easily owing to their relatively large size on CBCT images, the first branch of the Dental-YOLO output used a 13 × 13 low-scale feature map. MC is an object that is difficult to detect on CBCT images because it is small and sometimes invisible. Therefore, in this study, a 52 × 52 high-scale map feature was used to obtain better MC detection.

The Dental-YOLO detection process starts by dividing a 416 × 416 pixels input image into a grid size of 13 × 13. In each grid, three bounding boxes were generated to detect the objects. In each bounding box, a detection confidence value was generated to show the accuracy of the detection results for each object on the grid. The detection confidence value is zero if there are no objects in the grid. Otherwise, the detection confidence value is equal to the over union (*IoU*) intersection between the ground truth and bounding box. The confidence score threshold was used to determine which bounding box should be retained [21]. The bounding box with the highest detection confidence value is selected as the output of the detection process.

D. BONE HEIGHT AND WIDTH MEASUREMENT

The outputs of the detection process are the top–left coordinate (x, y) of the bounding box and the length and width of the object that can be detected in the image. The output values were used to calculate the height and width of available bone in the implant area. Bone height (*hBone*) is the distance between the crest of the bone and the MC [3]. In this study, *hBone* was calculated as the difference between the top y-coordinate value over the MC (top_yMC) and the top y-coordinate value over AB (top_yAB). An adjustment value for bone height (c_h) in millimeters was added to obtain *hBone* in line with the expert's calculations. The *hBone* equation proposed in this study is as in (1).

$$hBone = top_yMC - top_yAB + c_h \qquad (1)$$

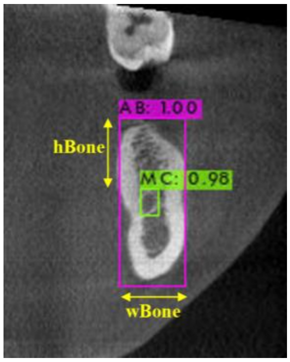

$top_yMC = 105$
$top_yAB = 65$
$widthAB = 37$ pixels
$c_h = c_w = 0$
$hBone = 40$ pixels = 12 mm
$wBone = 37$ pixels = 11.1 mm

FIGURE 5. Example of bone height and width measurement.

The alveolar process width determines the bone width (*wBone*) [4]. In this study, *wBone* was calculated from the width of the bounding box of AB (*widthAB*), as shown in (2). An adjustment value for bone width (c_w) in millimeters was added to obtain *wBone* in line with the expert's calculations.

$$wBone = widthAB + c_w \qquad (2)$$

Fig. 5 shows an example of measuring *hBone* and *wBone* of the available bone using the result of the Dental-YOLO detection. *hBone* is calculated using (1) with $c_h = 0$, such that *hBone* is obtained from the difference between top_yMC and top_yAB, which is 40 pixels. *wBone* is calculated using (2) with $c_w = 0$, so *wBone* equals *widthAB*, which is 37 pixels. The image resolution is 0.3 × 0.3 × 0.3 mm, meaning that 1 pixel in the image file equals 0.3 mm.

III. EXPERIMENTS AND RESULTS

A. EXPERIMENTAL DESIGN

The training process was performed to develop a detection model using Dental-YOLO. This process used 744 annotated 2D coronal slice grayscale images. The training process was performed up to a maximum batch of 4000. The batch size, learning rate, momentum, and decay used in the experiment were 64, 0.001, 0.9, and 0.0005, respectively. After the detection model was developed, 320 images were used for testing. The output of the detection process is used for the bone measurement process.

In this study, four implant areas with varying AB morphology were selected for bone measurement. In each implant area, several images that measured the height and width of the available bone were selected. Image selection was based on the implant site area in relation to neighboring teeth and the mesial-distal width AB for the ideal dental implant location, which is 3 mm [30]. Since the pixel spacing is 0.3 mm, five images in the mesial direction and five images in the distal direction were taken from the center image of the

TABLE II
PERFORMANCE COMPARISON OF DETECTION RESULT

Approach	mAP (%)	Avg IoU (%)	AP AB (%)	AP MC (%)	BFLOPS
YOLOv3	99.15	83.12	99.07	99.22	65.31
YOLOv3-tiny	97.58	78.50	99.04	96.12	5.45
YOLOv4	98.99	84.51	99.68	98.31	59.57
Dental-YOLO	**99.46**	**81.33**	**99.37**	**99.55**	**6.83**

implant site area, so that eleven images were selected for each implant area.

Two dental radiologists from the Airlangga University dental hospital performed manual bone measurements. The first radiologist, expert1, had 14 years of experience, while the expert2, had two years of experience. The two experts work individually and separately to take bone measurements using a CBCT viewer. The proposed approach measures bone using Equation 1 and 2, where previously the images were detected using Dental-YOLO. After measurement, the mean measurement of bone height and width in each implant area was calculated. These mean values were used to statistically compare the results of the two radiologists' bone measurements and the proposed method.

B. DETECTION PERFORMANCE

Detection performance was examined using the mean average precision (*mAP*), average intersection of union (*Avg IoU*), average precision (*AP*) for each class, and billions of floating-point operations (*BFLOPS*) required per second. The *mAP* score was calculated by calculating the mean *AP* across all the classes. *IoU* is a metric that measures the overlap between the ground truth and bounding box to determine the accuracy of an object detector. The higher the mAP and IoU values, the better the detection performance. BFLOPS was used to measure the computational time complexity of the number of model operations. The higher the BFLOPS requires higher computational power and a longer training process.

First, the detection performance of Dental-YOLO was compared with the YOLOv4, YOLOv3, and YOLOv3-tiny approaches. Table II lists the detection results, showing that the *mAP* and *AP* MC values using the Dental-YOLO approach were the best with values of 99.46% and 99.55%, respectively. The mAP and AP MC using the YOLOv4 approach were 98.99% and 98.31%, respectively. These results prove that the performance of Dental-YOLO detection is better than that of YOLOv4, especially in detecting MC. However, using the Dental-YOLO approach, the *Avg IoU* and *AP* of AB detection decreased compared with the original YOLOv4 approach. The Dental-YOLO approach's detection resulted in an *Avg IoU* of 81.33%, which was slightly reduced from YOLOv3 and YOLOv4 of 83.12% and 84.51%, respectively, but much higher than YOLOv3-tiny of 78.50%.

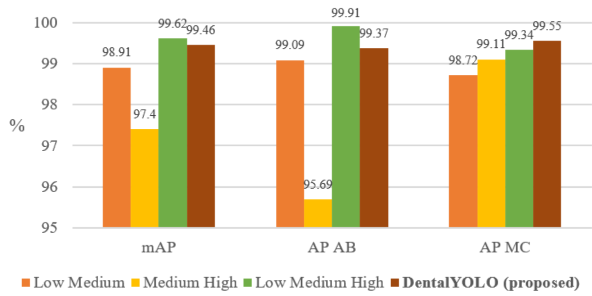

FIGURE 6. Detection results using different scales.

Dental-YOLO simplifies YOLOv4 architecture by significantly reducing the *BFLOPS* required from 59.57 to 6.83. The simplification of the architecture and feature map scale of the proposed approach made the detection process faster. Dental-YOLO and YOLOv3-tiny use two feature maps in the output branch. Therefore, *BFLOPS* is smaller than YOLOv3 and YOLOv4, respectively. Meanwhile, the network size in Dental-YOLO is more complex than that in YOLOv3-tiny, resulting in the *BFLOPS* of Dental-YOLO being larger than that of YOLOv3-tiny. The overall detection result of the proposed approach using the Dental-YOLO approach is better than that of the YOLOv3-tiny approach; both are tiny YOLO approaches, and the performance of the proposed approach is as good as that of YOLOv4.

Second, a performance comparison was performed by changing the feature map scale to analyze the detection performance with low- and high-scale feature maps on Dental-YOLO. The scale variations used were low and medium scales, medium and high scales, and a combination of low, medium, and high scales used by YOLOv4. Fig. 6 shows the performance results obtained using different scales. From the MC detection results, Dental-YOLO achieved the best result, with an *AP* MC of 99.55%. The use of low and medium scales resulted in the lowest mandibular detection, with an *AP* MC of 98.72%, compared with other scales that used high scales. These results indicate that high-scale feature maps are more suitable for MC detection. The use of low and high scales on the Dental-YOLO head architecture produces similar *mAP* and *AP* AB values using all scales (low, medium, and high). However, using two scales in Dental-YOLO is more efficient than using three scales. For AB detection results, the use of medium and high scales resulted in the lowest *mAP* and *AP* values compared with other scales that used low scales. Fig. 6 on *AP* AB shows the bar height on the medium-high scale, which is very low compared to the other scales. This shows that the combination of medium and high scales is unsuitable for detecting AB because AB is visible at low scales.

Fig. 7 shows examples of the AB and MC detection results using Dental-YOLO with variations in the shape and number of AB and MC. The image shows the detection results in the form of a bounding box on the AB and MC that were successfully detected, and the detection confidence value was written above the bounding box. All AB objects in the sample

This article has been accepted for publication in IEEE Access. This is the author's version which has not been fully edited and
content may change prior to final publication. Citation information: DOI 10.1109/ACCESS.2022.3208350

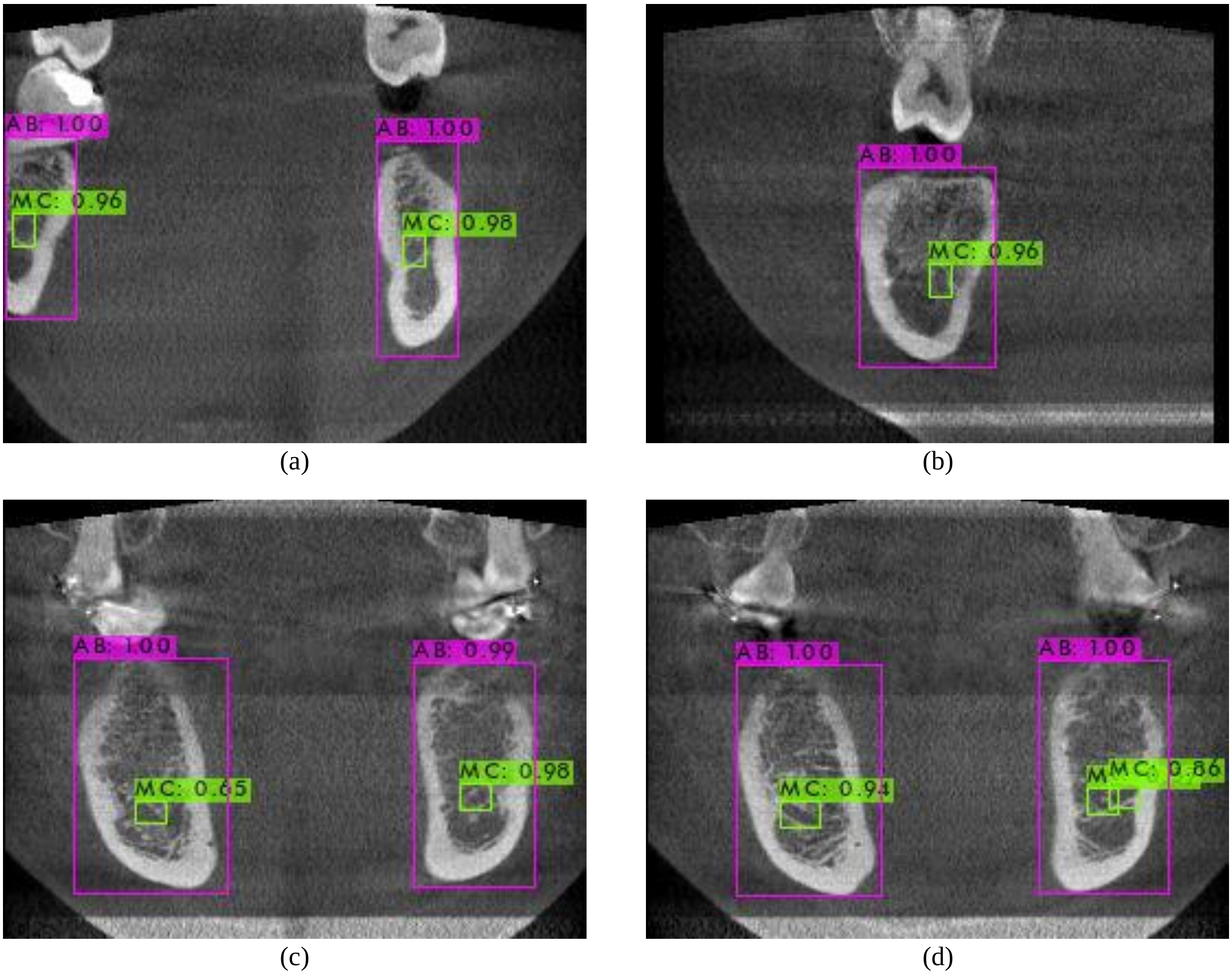

FIGURE 7. Examples of detection results.

were detected successfully, with a high confidence measurement because the size of AB was quite large and visible. For MC detection, the confidence value of the detection results depends on the clarity of the MC image. If it is clear, the confidence value is high (above 0.9), as shown in Fig. 7(a), (b), (c) on the right, and (d) on the left, the MC is a small sphere in AB. The MC is less clear in Fig. 7(c) on the left. Therefore, the confidence value is only 0.65. Meanwhile, in Fig. 7(d), there is a false-positive case in detecting the MC in the right bone as two adjacent MC objects. This is because the shape of the MC elongated from walls AB and inside AB.

The study detected AB using YOLOv3-tiny, resulting in *mAP* of 98.60% [27]. The difference between YOLOv3-tiny and Dental-YOLO lies in the backbone architecture; YOLOv3 uses Darknet53, whereas Dental-YOLO uses CSPDarknet. The use of CSP modules can improve the learning ability of convolution networks and increase their accuracy. Dental-YOLO achieved *AP* of 94.97% for AB detection, outperforming YOLOv3-tiny.

C. BONE MEASUREMENT

The *hBone* and *wBone* measurements of the proposed approach (*P*) were calculated using equations (1) and (2) and compared with the measurements made in expert1 (*E1*) and expert2 (*E2*). Table III shows the mean height (*Mh*) and mean width (*Mw*), as well as the difference in mean height (*MDh*) and difference in mean width (*MDw*) of the four bone implant areas. The mean difference (MD) was calculated from the difference in the mean measurement between the expert (*MDhE* and *MDwE*) and the difference in the mean measurement between the expert and the proposed (*MDhE1P*, *MDhE2P*, *MDwE1P*, and *MDwE2P*). The MD column for each height and width measurement also displayed the smallest value (*min*), largest value (*max*), and range between the smallest and largest MD values (*range*). In this study, the c_h value for the *hBone* measurement was -1, and the c_w for the *wBone* measurement was -0.3.

Table III shows MD among experts was small for measurements of bone height (*MDhE*) and width (*MDwE*).

TABLE III
MEAN AND MEAN DIFFERENCE (MD) IN BONE HEIGHT AND WIDTH MEASUREMENTS

	Mean bone height (mm)						Mean bone width (mm)					
Implant area	*MhE1*	*MhE2*	*MhP*	*MDhE*	*MDhE1P*	*MDhE2P*	*MwE1*	*MwE2*	*MwP*	*MDwE*	*MDwE1P*	*MDwE2P*
1	10.99	10.98	10.89	**0.01**	0.10	**0.09**	11.36	11.13	11.26	0.23	**0.10**	**0.13**
2	11.66	11.51	12.64	0.15	0.98	1.13	18.81	18.64	18.33	0.17	0.48	0.31
3	17.02	16.83	17.05	0.19	**0.03**	0.22	14.86	14.71	17.75	0.15	2.89	3.04
4	16.38	16.28	16.54	0.10	0.16	0.26	15.43	15.37	19.88	**0.06**	4.45	4.51
min				0.01	0.03	0.09				0.06	0.10	0.13
max				0.19	0.98	1.13				0.23	4.45	4.51
range				0.18	0.95	1.04				0.17	4.35	4.38

The *range* of MD indicates that the measurement of bone height has a smaller MD than that of bone width.

D. STATISTICAL ANALYSIS

Bone measurements were evaluated by two-way ANOVA using the Minitab 19. Two-way ANOVA was performed to test whether there was a difference in the measurement between the proposed approach and the experts. Two independent variables were analyzed for their significance in the measurement of mean bone height and width. The first variable is the *system*, which is the object that takes the measurements and consists of the proposed approach, expert1, and expert2. The second variable is the *implant area*, which comprises four implant areas where measurements are taken, namely implant areas 1, 2, 3, and 4. Fig. 8 shows bones with various AB morphology variations from each implant area.

Tables IV and V show the results of the two-way ANOVA test for the measurement of bone height and width, respectively, from Minitab19. The significance level (α) used in the two-way ANOVA test was 0.05. For the *system* variable, the p-value obtained from the measurement of bone height was 0.249, and that of bone width was 0.184, both of which were greater than 0.05. This means that the *system* variable had no significant effect on the bone height and width measurements. It can be concluded that there is no difference in the measurement of bone height and width produced by the proposed approach and experts. As for the *implant area* variable, the p-value of bone height measurement was 0.000 and bone width measurement was 0.003, both of which were smaller than 0.05. This means that the *implant area* variable significantly affects the measurement of the bone height and width.

TABLE IV
RESULT OF TWO-WAY ANOVA FOR BONE HEIGHT MEASUREMENTS

Source	DF	Adj SS	Adj MS	F-value	P-value
System	2	0.305	0.152	1.77	**0.249**
Implant area	3	84.254	28.084	325.69	**0.000**
Error	6	0.517	0.086		
Total	11	85.075			

TABLE V
RESULT OF TWO-WAY ANOVA FOR BONE WIDTH MEASUREMENTS

Source	DF	Adj SS	Adj MS	F-value	P-value
System	2	8.367	4.183	2.27	**0.184**
Implant area	3	88.747	29.582	16.09	**0.003**
Error	6	11.034	1.839		
Total	11	108.146			

Analysis after the two-way ANOVA was performed for variables with p-values ≤ 0.05. Tukey's test was used to determine the *implant area* variable group based on mean bone height and width. Tables VI and VII show the grouping information using Tukey's analysis for measuring bone height and width from Minitab 19. From the information on the implant area group for measuring bone height, implant areas 3 and 4 were in the same group, whereas areas 2 and 1 were in separate groups. Meanwhile, the group information for measuring bone width showed that implant areas 2, 4, and 3 were in the same group, and area 1 was in another group.

The results of the two-way ANOVA test showed that there was no difference in bone height and width measurements produced by the proposed approach and the experts. This indicates that the proposed approach can be used to measure the available bone in the implant area. This means that the bounding box attribute of AB and MC detection from Dental-YOLO can be used for bone measurement in dental implant planning.

However, the implant area affects the measurement of bone height and width. This is due to the different morphologies of AB in the measured implant area. Fig. 8 displays the bone

TABLE VI
GROUPING INFORMATION USING THE TUKEY METHOD FOR MEASURING BONE HEIGHT

Implant area	N	Mean	Grouping		
3	3	16.967	**A**		
4	3	16.400	**A**		
2	3	11.937		**B**	
1	3	10.953			**C**

TABLE VII
GROUPING INFORMATION USING THE TUKEY METHOD FOR MEASURING BONE WIDTH

Implant area	N	Mean	Grouping	
2	3	18.593	**A**	
4	3	16.893	**A**	
3	3	15.773	**A**	
1	3	11.250		**B**

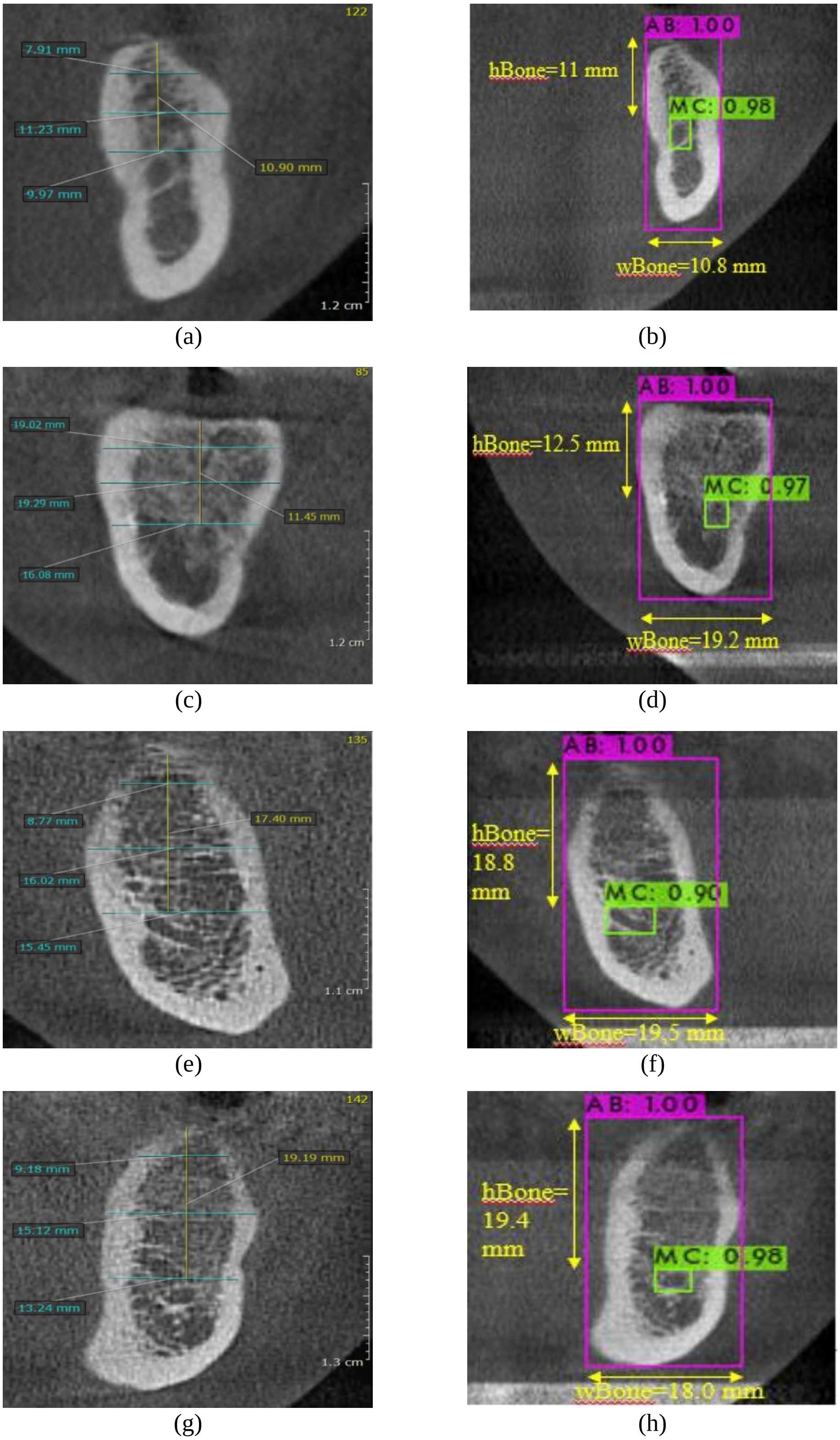

FIGURE 8. Height and width bone measurement by expert1 and proposed approach; (a) and (b) implant area 1 - region 36, (c) and (d) implant area 2 - region 47, (e) and (f) implant area 3 - region 46, (g) and (h) implant area 4 – region 36.

measurement results for four implant areas with varying AB morphology from expert1 and the proposed approach. AB in implant areas 3 and 4 had a similar bone morphology to the bone in areas 1 and 2. Implant areas 3 and 4 were in the same group, based on the grouping results for bone height and width. Implant area 1 has AB, which is narrower in width than other implant areas; therefore, it is in a separate group in the measurement of bone width. The bone measurements shown in Table III indicate that the MD bone height in implant area 1 was the smallest. The bone crest of implant area 1 was not reduced, and the bone position was upright so that the bone crest was at the top of the bounding box. Fig. 8(a) shows the expert1 *hBone* measurement at area 1 of 10.90 mm. Fig. 8(b) shows the *hBone* of the proposed approach of 11 mm. The measurement difference was 0.1 mm. In contrast, the MD bone height in implant area 2 was the highest. Fig. 8(c) and (d) show 2D CBCT images in the implant area 2. In these images, the bone crest decreased owing to bone loss. The top of the bone area was below the top of the bounding box AB. Fig. 8(c) shows the expert1 *hBone* measurement in area 2 of 11.45 mm and (d) shows the proposed approach of 12.5 mm. The measurement difference was 1.05 mm. A decrease in the AB bone peak affected the *hBone* measurement value.

Three measurements were performed by each expert to determine the available bone width. The experts chose the largest of the three bone width measurements as *wBone*. Fig. 8(a) shows the *wBone* value obtained by expert1 of 11.23 mm. The proposed *wBone* measurement in this study measures the width of AB from the width of the bounding box AB. Fig. 8(b) shows the *wBone* value of 10.8 mm. Table III shows that in the measurement of bone width, the MD in width for implants 1 and 2 is less than 1 mm, while the area for implants 3 and 4 is more than 3 mm. Fig. 8(a) to (d) show 2D CBCT images for implant areas 1 and 2. As shown in the figure, the AB bones are in an upright position such that the measured available bone width corresponds to the width of the AB bounding box. The width measurements were similar to the expert measurements. Fig. 8(e) to (h) show images of the implant areas 3 and 4, respectively. In the pictures, it can be seen that the shape of AB is not perpendicular. Therefore, the width of the bounding box AB is larger than the actual bone width. This causes the bone width measurement of the proposed approach to be larger than that of expert measurement.

Further research is needed to measure the height and width of the AB more precisely to reduce the MD in the bone height and width. AB crest detection can be applied to obtain a more precise *hBone*, especially in bones with decreased AB crest. The AB segmentation process can be applied to obtain a more precise *wBone* size, with the *wBone* measurement performed from the edge of AB.

IV. CONCLUSION

Dental-YOLO is a compressed version of YOLOv4 that successfully detects AB and MC simultaneously, using low- and high-scale features. Dental-YOLO has an average detection precision of 99.46%. Dental-YOLO detection was eight times faster than that using the YOLOv4 approach. Dental-YOLO's *BFLOPS* was 6.83, which was significantly smaller than that of YOLOv4's *BFLOPS* of 59.57. The training process becomes much more efficient. This greatly helps the efficiency of the development of the Dental-YOLO system in implant treatment planning.

The ANOVA test, which analyzes the comparison between the measurement results by the system and the radiologists, shows that automatic AB and MC detection can be used to properly measure the available bone in the implant area. There was shown to be no significant difference between the radiologist's measurements and the proposed method. Therefore, automated measurements can be used to simplify dental implant planning. However, further research is needed to improve the accuracy of bone measurement through the detection of AB crest and segmentation of the AB on dental CBCT images.

REFERENCES

[1] M. Bae, J. W. Park, and N. Kim, "Fully automated estimation of arch forms in cone-beam CT with cubic B-spline approximation: Evaluation of digital dental models with missing teeth," *Comput. Biol. Med.*, vol. 131, p. 104256, 2021, doi: 10.1016/j.compbiomed.2021.104256.

[2] P. Worthington, J. Rubenstein, and D. C. Hatcher, "The role of cone-beam computed tomography in the planning and placement of implants," *J. Am. Dent. Assoc.*, vol. 141 Suppl, pp. 19S-24S, 2010, doi: 10.14219/jada.archive.2010.0358.

[3] R. Jacobs, B. Salmon, M. Codari, B. Hassan, and M. M. Bornstein, "Cone beam computed tomography in implant dentistry: Recommendations for clinical use," *BMC Oral Health*, vol. 18, no. 1, pp. 1–17, 2018, doi: 10.1186/s12903-018-0523-5.

[4] G. Juodzbalys and M. Kubilius, "Clinical and Radiological Classification of the Jawbone Anatomy in Endosseous Dental Implant Treatment," *J. Oral Maxillofac. Res.*, vol. 4, no. 2, 2013, doi: 10.5037/jomr.2013.4202.

[5] M. L. Sun *et al.*, "Application of machine learning to stomatology: A comprehensive review," *IEEE Access*, vol. 8, pp. 184360–184374, 2020, doi: 10.1109/ACCESS.2020.3028600.

[6] J. Jaskari *et al.*, "Deep Learning Method for Mandibular Canal Segmentation in Dental Cone Beam Computed Tomography Volumes," *Sci. Rep.*, vol. 10, no. 1, pp. 1–9, 2020, doi: 10.1038/s41598-020-62321-3.

[7] R. H. Putra, C. Doi, N. Yoda, E. R. Astuti, and K. Sasaki, "Current applications and development of artificial intelligence for digital dental radiography," *Dentomaxillofacial Radiol.*, vol. 51, no. 1, 2022, doi: 10.1259/dmfr.20210197.

[8] X. Hu *et al.*, "Real-time detection of uneaten feed pellets in underwater images for aquaculture using an improved YOLO-V4 network," *Comput.*

Electron. Agric., vol. 185, no. September 2020, p. 106135, 2021, doi: 10.1016/j.compag.2021.106135.

[9] Y. Bayraktar and E. Ayan, "Diagnosis of interproximal caries lesions with deep convolutional neural network in digital bitewing radiographs," *Clin. Oral Investig.*, 2021, doi: 10.1007/s00784-021-04040-1.

[10] H. J. Chang *et al.*, "Deep Learning Hybrid Method to Automatically Diagnose Periodontal Bone Loss and Stage Periodontitis," *Sci. Rep.*, vol. 10, no. 1, pp. 1–9, 2020, doi: 10.1038/s41598-020-64509-z.

[11] Y. Miki *et al.*, "Classification of teeth in cone-beam CT using deep convolutional neural network," *Comput. Biol. Med.*, vol. 80, pp. 24–29, 2017, doi: 10.1016/j.compbiomed.2016.11.003.

[12] Z. Cui *et al.*, "A fully automatic AI system for tooth and alveolar bone segmentation from cone-beam CT images," *Nat. Commun.*, vol. 13, no. 1, pp. 1–11, 2022, doi: 10.1038/s41467-022-29637-2.

[13] R. Indraswari, A. Z. Arifin, N. Suciati, E. R. Astuti, and T. Kurita, "Automatic segmentation of mandibular cortical bone on cone-beam CT images based on histogram thresholding and polynomial fitting," *Int. J. Intell. Eng. Syst.*, vol. 12, no. 4, pp. 130–141, 2019, doi: 10.22266/ijies2019.0831.13.

[14] G. H. Kwak *et al.*, "Automatic mandibular canal detection using a deep convolutional neural network," *Sci. Rep.*, vol. 10, pp. 1–9, 2020, doi: 10.1038/s41598-020-62586-8.

[15] P. Lahoud *et al.*, "Development and validation of a novel artificial intelligence driven tool for accurate mandibular canal segmentation on CBCT," *J. Dent.*, vol. 116, no. October 2021, p. 103891, 2022, doi: 10.1016/j.jdent.2021.103891.

[16] S. Lee, S. Woo, J. Yu, J. Seo, J. Lee, and C. Lee, "Automated CNN-Based tooth segmentation in cone-beam CT for dental implant planning," *IEEE Access*, vol. 8, pp. 50507–50518, 2020, doi: 10.1109/ACCESS.2020.2975826.

[17] R. Indraswari, T. Kurita, A. Z. Arifin, N. Suciati, and E. R. Astuti, "Multi-projection deep learning network for segmentation of 3D medical images," *Pattern Recognit. Lett.*, vol. 125, pp. 791–797, 2019, doi: 10.1016/j.patrec.2019.08.003.

[18] H. K. Lim, S. K. Jung, S. H. Kim, Y. Cho, and I. S. Song, "Deep semi-supervised learning for automatic segmentation of inferior alveolar nerve using a convolutional neural network," *BMC Oral Health*, vol. 21, no. 1, pp. 1–9, 2021, doi: 10.1186/s12903-021-01983-5.

[19] J. Redmon, S. Divvala, R. Girshick, and A. Farhadi, "You only look once: Unified, real-time object detection," *Proc. IEEE Comput. Soc. Conf. Comput. Vis. Pattern Recognit.*, vol. 2016-Decem, pp. 779–788, 2016, doi: 10.1109/CVPR.2016.91.

[20] J. Redmon and A. Farhadi, "YOLO9000: Better, faster, stronger," *Proc. - 30th IEEE Conf. Comput. Vis. Pattern Recognition, CVPR 2017*, pp. 6517–6525, 2017, doi: 10.1109/CVPR.2017.690.

[21] J. Redmon and A. Farhadi, "YOLOv3: An incremental improvement," *arXiv*, 2018.

[22] A. Bochkovskiy, C.-Y. Wang, and H.-Y. M. Liao, "YOLOv4: Optimal Speed and Accuracy of Object Detection," 2020, [Online]. Available: http://arxiv.org/abs/2004.10934.

[23] Z. Zhuang *et al.*, "Cardiac VFM visualization and analysis based on YOLO deep learning model and modified 2D continuity equation," *Comput. Med. Imaging Graph.*, vol. 82, p. 101732, 2020, doi: 10.1016/j.compmedimag.2020.101732.

[24] T. Ozturk, M. Talo, E. A. Yildirim, U. B. Baloglu, O. Yildirim, and U. Rajendra Acharya, "Automated detection of COVID-19 cases using deep neural networks with X-ray images," *Comput. Biol. Med.*, vol. 121, no. April, p. 103792, 2020, doi: 10.1016/j.compbiomed.2020.103792.

[25] G. H. Aly, M. Marey, S. A. El-Sayed, and M. F. Tolba, "YOLO Based Breast Masses Detection and Classification in Full-Field Digital Mammograms," *Comput. Methods Programs Biomed.*, vol. 200, p. 105823, 2021, doi: 10.1016/j.cmpb.2020.105823.

[26] S. Albahli, N. Nida, A. Irtaza, M. H. Yousaf, and M. T. Mahmood, "Melanoma Lesion Detection and Segmentation Using YOLOv4-DarkNet and Active Contour," *IEEE Access*, vol. 8, pp. 198403–198414, 2020, doi: 10.1109/ACCESS.2020.3035345.

[27] M. Widiasri, A. Z. Arifin, N. Suciati, E. R. Astuti, and R. Indraswari, "Alveolar Bone Detection from Dental Cone Beam Computed Tomography using YOLOv3-tiny," pp. 1–6, 2021, doi: 10.1109/aims52415.2021.9466037.

[28] P. Xu *et al.*, "On-board real-time ship detection in hisea-1 sar images based on cfar and lightweight deep learning," *Remote Sens.*, vol. 13, no. 10, pp. 1–18, 2021, doi: 10.3390/rs13101995.

[29] X. Li, T. Lai, S. Wang, Q. Chen, C. Yang, and R. Chen, "Weighted feature pyramid networks for object detection," *Proc. - 2019 IEEE Intl Conf Parallel Distrib. Process. with Appl. Big Data Cloud Comput. Sustain. Comput. Commun. Soc. Comput. Networking, ISPA/BDCloud/SustainCom/SocialCom 2019*, pp. 1500–1504, 2019, doi: 10.1109/ISPA-BDCloud-SustainCom-SocialCom48970.2019.00217.

[30] A. Cristoforetti *et al.*, "Assessing the accuracy of computer-planned osteotomy guided by stereolithographic template: A methodological framework applied to the mandibular bone harvesting," *Comput. Biol. Med.*, vol. 114, 2019, doi: 10.1016/j.compbiomed.2019.103435.

This article has been accepted for publication in IEEE Access. This is the author's version which has not been fully edited and content may change prior to final publication. Citation information: DOI 10.1109/ACCESS.2022.3208350

MONICA WIDIASRI (Member, IEEE) received her bachelor's degree in Computer Science from Institut Teknologi Sepuluh Nopember in 2001 and master's degree in Computer Science from Institut Teknologi Sepuluh Nopember in 2012. She currently became a doctoral student in Institut Teknologi Sepuluh Nopember. She is a lecturer in Universitas Surabaya since 2003. Her researh interest includes artificial intelligence, deep learning, computer vision, and pattern recognition.

AGUS ZAINAL ARIFIN received his bachelor's degree in Computer Science from Institut Teknologi Sepuluh Nopember in 1995, master's degree in Computer Science from Universitas Indonesia in 2001, and doctoral degree in Information Engineering from Hiroshima University in 2007. He has been a lecturer in the Department of Informatics, Institut Teknologi Sepuluh Nopember since 1995. He is among the top 500 authors based on the SINTA Score 2020. His research interests include image processing, particularly in medical imaging, machine learning, deep learning, and information retrieval. Since May 2021, he has been the head of the Center for Social Welfare Data and Information of the Ministry of Social Affairs of the Republic of Indonesia.

NANIK SUCIATI (Member, IEEE) received her master's degree in computer science from the University of Indonesia, in 1998, and the Dr. Eng. degree in Information Engineering from the University of Hiroshima, in 2010. She is currently an associate professor at the Department of Informatics, Institut Teknologi Sepuluh Nopember. She has published more than 50 journal articles and conference papers on computer science. Her research interests include computer vision, computer graphics, and artificial intelligence.

CHASTINE FATICHAH (Member, IEEE) received the Ph.D. degree from the Tokyo Institute of Technology, Japan, in 2012. She is currently an Associate Professor with the Institut Teknologi Sepuluh Nopember, Surabaya, Indonesia. She has published more than 110 journal articles and conference papers related to computer science. Her research interests include artificial intelligence, image processing, and data mining.

EHA RENWI ASTUTI received doctoral degree in Health Science from Universitas Airlangga Faculty of Medicine post-graduate course, Indonesia, in 2005. She is currently an associate professor at the Department of Dentomaxillofacial Radiology, Universitas Airlangga, Indonesia. Since 2008, she has been working as an oral radiologist at Universitas Airlangga Academic Dental Hospital, Indonesia. Her research interests include radiographic imaging, artificial intelligence in dental radiography, radioprotective agents, radiology in forensic odontology, and radiation biology.

RARASMAYA INDRASWARI (Member, IEEE) received her bachelor's degree in Computer Science from Institut Teknologi Sepuluh Nopember in 2015, master's degree in Computer Science from Institut Teknologi Sepuluh Nopember, and doctoral degree in Computer Science from Institut Teknologi Sepuluh Nopember in March 2020. She is a lecturer in the Department of Information Systems in Institut Teknologi Sepuluh Nopember. Her research interests include data mining, machine learning, image processing, and computer vision.

RAMADHAN HARDANI PUTRA received the PhD degree in Dental Science from Tohoku University Graduate School of Dentistry, Japan, in 2021. He is currently a lecturer at the Department of Dentomaxillofacial Radiology, Universitas Airlangga, Indonesia. His research interests include dental implant, digital dentistry, radiographic imaging, and artificial intelligence in dental radiography.

CHOIRU ZA'IN received his doctoral degree from the School of Computing, Engineering, and Mathematical Science at La Trobe University Melbourne in 2020. He is with Monash University as a research associate and sessional Lecturer in the Faculty of Information Technology. His research interest is arge-scale data stream analysis, and he has published in many high-quality journals in computer science. He has also been involved in reviewing many reputable journals.